PHYSICAL REVIEW D **84,** 095025 (2011)

Gluon-fusion contributions to Φ+2 jet production

F. Campanario,[1] M. Kubocz,[2] and D. Zeppenfeld[1]

[1]*Institut für Theoretische Physik, Universität Karlsruhe P. O. Box 6980 76128 Karlsruhe, Germany*

[2]*Institut für Theoretische Teilchenphysik und Kosmologie, RWTH Aachen University, D52056 Aachen, Germany*

(Received 30 November 2010; published 21 November 2011)

In high energy hadronic collisions, a scalar or pseudoscalar Higgs boson, $\Phi = H, A$, can be efficiently produced via gluon fusion, which is mediated by heavy quark loops. In this paper, we consider double real emission corrections to $\Phi = A$ production, which lead to a Higgs plus two-jet final state, at order α_s^4. Full quark mass effects are considered in the calculation of scattering amplitudes for the $\mathcal{CP}$-odd Higgs boson A, as induced by quark triangle-, box-, and pentagon-diagrams. They complement the analogous results for a $\mathcal{CP}$-even Higgs boson H in Ref. [1]. Interference effects between loops with top and bottom quarks as well as between $\mathcal{CP}$-even and $\mathcal{CP}$-odd couplings of the heavy quarks are fully taken into account.

DOI: 10.1103/PhysRevD.84.095025 PACS numbers: 14.80.Ec, 14.80.Da

I. INTRODUCTION

One of the prime tasks of the CERN Large Hadron Collider (LHC) is the search for the origins of the spontaneous breaking of the electroweak $SU(2) \times U(1)$ gauge symmetry and, once such particles are found, the study of one or several Higgs bosons as the remnants of the symmetry breaking mechanism. Among the various Higgs boson production channels, the gluon fusion and the weak boson fusion processes have emerged as the most promising channels for Higgs boson discovery at the LHC [1–3], and they are equally valuable for the study of its properties, like the measurement of its couplings to gauge boson and fermions [4,5].

In weak boson fusion (WBF), $qq \to qqH$ mediated by t-channel W or Z exchange, the two forward tagging jets arising from the scattered quarks provide a tell-tale signature which can be used for efficient background rejection [6]. The same Hjj signature can also arise in gluon-fusion events, via $\mathcal{O}(\alpha_s^2)$ real emission corrections to $gg \to H$ which, within the standard model (SM), is mediated mainly by a top quark loop. For a Higgs boson, which is lighter than the top quark, the resulting Hjj cross section can be determined to good approximation by an effective Lagrangian of energy dimension five, which is given by [7–12]

$$\mathcal{L}_{\text{eff}} = \frac{y_t}{y_t^{\text{SM}}} \cdot \frac{\alpha_s}{12\pi v} \cdot H G^a_{\mu\nu} G^{a\mu\nu} + \frac{\tilde{y}_t}{y_t^{\text{SM}}} \cdot \frac{\alpha_s}{8\pi v} \cdot A G^a_{\mu\nu} \tilde{G}^{a\mu\nu}, \tag{1.1}$$

where $G^a_{\mu\nu}$ denotes the gluon field strength and $\tilde{G}^{a\mu\nu} = 1/2 G^a_{\rho\sigma} \varepsilon^{\mu\nu\rho\sigma}$ its dual. The two terms result from a $\bar{t}tH$ and a $\bar{t}i\gamma_5 tA$ coupling of the (pseudo) scalar Higgs, respectively, and they lead to distinctively different distributions of the azimuthal angle between the two jets: the $\mathcal{CP}$-even Hgg coupling produces a minimum for $\phi_{jj} = \pm\pi/2$, while a $\mathcal{CP}$-odd Agg coupling leads to minima at $\phi_{jj} = 0$ and $\pm\pi$. These distinctions become important in two-Higgs-doublet models (2HDM) like the minimal supersymmetric extension of the standard model (MSSM), where a $\mathcal{CP}$-odd Higgs, A, appears in addition to a light and a heavy, neutral $\mathcal{CP}$-even Higgs, h and H: the azimuthal angle distribution of Φjj events allow to differentiate between a $\mathcal{CP}$-even Higgs ($\Phi = h, H$) or a $\mathcal{CP}$-odd one ($\Phi = A$).

For large Higgs boson masses ($m_H \gtrsim m_t$), the full quark mass dependence of the loop diagrams must be calculated for reliable predictions, and the same is true for large ratios of the two vacuum expectation values, $v_u/v_d = \tan\beta$, where bottom-quark loops provide the dominant contributions to $qq \to qqH$, $qg \to qgH$, and $gg \to ggH$ amplitudes. For a $\mathcal{CP}$-even Higgs boson, these calculations were performed in Ref. [13]. The purpose of the present paper is to present the corresponding results for a $\mathcal{CP}$-odd Higgs boson, $\Phi = A$, or more precisely, for an underlying Higgs coupling to quarks derived from the Yukawa Lagrangian $\mathcal{L} = y_q \bar{q} i\gamma_5 q A$. By combining the present results with those for a $\mathcal{CP}$-even Higgs, the quark-loop-induced contributions to Φjj production can be calculated for an arbitrary Yukawa coupling of the form

$$\mathcal{L}_{\text{Yukawa}} = \bar{q}(y_q + i\gamma_5 \tilde{y}_q) q \Phi. \tag{1.2}$$

Our results are implemented in a parton level Monte Carlo program which is part of the VBFNLO program package [14]. This numerical implementation allows to calculate Φjj production cross sections in hadronic collisions including top- and bottom-quark loop contributions for arbitrary combinations of the Yukawa couplings y_q and $\tilde{y}_q$ ($q = t, b$).

Our paper is organized as follows. In Sec. II, we first define the models in which we consider pseudoscalar Higgs production. We then provide an outline of the calculation of the scattering amplitudes for the three basic subprocesses, $qq \to qqA$, $qg \to qgA$, and $gg \to ggA$. Further details on the various loop contributions are relegated to the Appendixes. We have performed a number of analytic and numerical consistency checks on our calculation: they are described in Sec. III. The main phenomenological results

are presented in Sec. IV, for pp scattering at the LHC with a center of mass energy of $\sqrt{s} = 14$ TeV. For various combinations of top- and bottom-quark contributions, parameterized by $\tan\beta$, we provide integrated Ajj cross sections but also differential distributions. Results are also presented for general Φjj events, i.e. for the production of a Higgs boson with arbitrary $\mathcal{CP}$-violating couplings to the third generation quarks. Final conclusions are drawn in Sec. V.

II. OUTLINE OF THE CALCULATION AND MATRIX ELEMENTS

The production of the $\mathcal{CP}$-odd Higgs boson A in association with two jets, at order α_s^4, proceeds in analogy to the production of the $\mathcal{CP}$-even Higgs boson $H_{\rm SM}$ of the SM. The $H_{\rm SM}jj$ production processes with full heavy quark mass effects were considered in Ref. [13], and we closely follow the framework and the notation introduced there. We consider the production subprocesses

$$qq \to qqA, \quad qQ \to qQA, \quad qg \to qgA, \quad gg \to ggA, \tag{2.1}$$

and all crossing-related processes. Here, the first two entries denote scattering of identical and nonidentical quark flavors. The Higgs boson A is produced by massive quark loops, for which only the third quark generation is taken into account. Furthermore, within the MSSM, massive squark loops can safely be neglected, because their contribution sums to zero at amplitude level in the production of a $\mathcal{CP}$-odd Higgs boson [15]. In the 2HDM, up- and down-type quark Yukawa couplings depend on the ratio of vacuum expectation values, $\tan\beta = v_u/v_d$, via the relations

(1) 2HDM of type I:

$$\tilde{y}^{\rm I}_{A,uu} = \frac{\cot\beta}{v} m_u \quad \text{and} \quad \tilde{y}^{\rm I}_{A,dd} = -\frac{\cot\beta}{v} m_d, \tag{2.2}$$

(2) 2HDM of type II (MSSM):

$$\tilde{y}^{\rm II}_{A,uu} = -\frac{\cot\beta}{v} m_u \quad \text{and} \quad \tilde{y}^{\rm II}_{A,dd} = -\frac{\tan\beta}{v} m_d. \tag{2.3}$$

In the 2HDM of type I, Yukawa couplings for up-type and down-type quarks are suppressed equally at large $\tan\beta$ compared to the 2HDM of type II, where only the up-type Yukawa coupling is suppressed but the down-type Yukawa coupling is enhanced. Because of this enhancement, loops with bottom quarks can also provide significant contributions to cross sections.

In the calculation of the subprocesses listed in (2.1), three different loop topologies appear: the triangle, box, and pentagon diagrams of Fig. 1. The contributing Feynman diagrams can be easily built from the simpler QCD dijet processes at leading order. One needs to insert the Higgs-gluon triangles into the gluon propagators of the $2 \to 2$ tree-level diagrams in all possible ways or one replaces a triple gluon or four gluon vertex by box or pentagon graphs in all possible ways. Charge-conjugation related diagrams, where the loop momentum is running clockwise and counterclockwise, can be counted as one by exploiting Furry's theorem [16]. This effectively reduces the number of diagrams by a factor of 2. Furthermore, all diagrams are UV-convergent and, due to the finite quark mass in the loops, also IR-convergent. All coupling constants and loop factors which appear can conveniently be absorbed into an overall factor

$$F_f = 4 m_f h_f \frac{g_s^4}{16\pi^2} = 4 m_f h_f \alpha_s^2, \tag{2.4}$$

where $f = b, t$ labels the heavy quark flavor of a particular loop. In the following, we use the MSSM couplings of Eq. (2.3), i.e. we set $h_t = \cot\beta m_t/v$ and $h_b = \tan\beta m_b/v$. By pulling out a loop factor $4m_f/16\pi^2$, we anticipate that the Dirac trace of all loops requires a quark mass insertion to compensate the helicity flip induced by the $\Phi f\bar{f}$ coupling.

1. Subprocesses $qQ \to qQA$ and $qq \to qqA$

The subprocess $qQ \to qQA$, depicted in Fig. 1(a), is the simplest contribution to $A + 2$ jet production. Following Ref. [13], the amplitude for different flavors can be written as

$$\begin{aligned} \mathcal{A}^{qQ} &= \sum_{f=t,b} F_f^{qQ} J_{21}^{\mu_1} J_{43}^{\mu_2} T_{\mu_1\mu_2}(q_1, q_2, m_f) t^a_{i_2 i_1} t^a_{i_4 i_3} \\ &= \mathcal{A}^{qQ}_{2143} t^a_{i_2 i_1} t^a_{i_4 i_3}. \end{aligned} \tag{2.5}$$

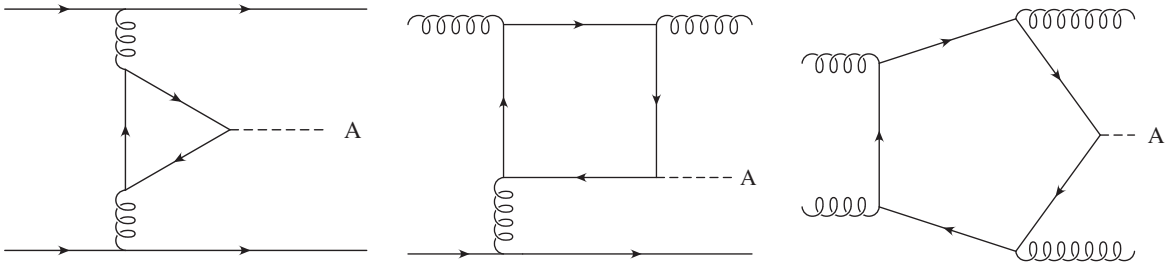

FIG. 1. Examples of Feynman graphs contributing to $A + 2$ jet production via gluon fusion.

Using the notation and formalism for the spinor algebra of [17], the external quark lines can be expressed by effective quark currents $J_{21}^{\mu_1}$ and $J_{43}^{\mu_2}$ as given in [13]. The triangle tensor $T^{\mu_1\mu_2}(q_1, q_2, m_f)$ (see Appendix A Fig. 10) has the simple form

$$T^{\mu_1\mu_2}(q_1, q_2, m_f) = \varepsilon^{\mu_1\mu_2 q_1 q_2} C_0(q_1, q_2, m_f). \quad (2.6)$$

Here, C_0 denotes the scalar three-point function and $\varepsilon^{\mu_1\mu_2 q_1 q_2}$ is the totally antisymmetric tensor (Levi-Civita symbol) in four dimensions contracted with attached gluon momenta q_1 and q_2. The $t_{ij}^a = \lambda_{ij}^a/2$ are color generators in the fundamental representation of $SU(N)$, $N = 3$ and the overall factor

$$F_f^{qQ} = S_1 S_2 S_3 S_4 4\sqrt{\bar{p}_1^0 \bar{p}_2^0 \bar{p}_3^0 \bar{p}_4^0} F_f \quad (2.7)$$

includes normalization factors of external quark spinors. Here, the $\bar{p}_i$ denote physical momenta describing phase space and the wave functions of fermions and bosons while p_i is used for momenta appearing in the momentum flow in Feynman diagrams. Both sets of momenta are related by the sign factors S_i [17]

$$p_i = S_i \bar{p}_i, \quad (2.8)$$

with $S_i = +1$ for fermions and $S_i = -1$ for anti-fermions. The factor F_f is given in Eq. (2.4). For identical quark flavors, one has to keep in mind Pauli interference

$$\mathcal{A}^{qq} = \mathcal{A}^{qq}_{2143} t^a_{i_2 i_1} t^a_{i_4 i_3} - \mathcal{A}^{qq}_{4123} t^a_{i_4 i_1} t^a_{i_2 i_3}. \quad (2.9)$$

The squared amplitude, summed over initial- and final-particle color, becomes

$$\sum_{\text{color}} |\mathcal{A}^{qq}|^2 = (|\mathcal{A}_{2143}|^2 + |\mathcal{A}_{4123}|^2)\frac{N^2-1}{4} + 2\,\text{Re}(\mathcal{A}_{2143}\mathcal{A}^*_{4123})\frac{N^2-1}{4N}. \quad (2.10)$$

2. Subprocesses $qg \to qgA$

Polarization vectors of external gluon lines with a triangle insertion can be expressed by effective polarization vectors

$$e^\mu_{iA}(m_f) = \varepsilon^{\mu\epsilon_i q_i P}\frac{1}{(q_i+P)^2} C_0(q_i, -(q_i+P), m_f), \quad (2.11)$$

which replace the polarization vectors ϵ_i^μ of the underlying $2 \to 2$ process for gluons $i = 1, 2$. Here, q_i is the external gluon momentum while P denotes the momentum of the Higgs boson. The expression for the amplitude of graphs with a triangle insertion adjacent to a three-gluon vertex differs slightly from that in [13] due to the emergence of the Levi-Civita symbol

$$\mathcal{A}^{qg}_{\text{tri}} = \sum_f F_f^{qg}[t^{a_1}, t^{a_2}]_{i_1 i_2}\Big\{2[e_{1A}\cdot\epsilon_2 J_{21}\cdot q_2 - e_{1A}\cdot J_{21}\epsilon_2\cdot(p_2-p_1) - e_{1A}\cdot q_2 J_{21}\cdot\epsilon_2] - 2[e_{2A}\cdot\epsilon_1 J_{21}\cdot q_1 - e_{2A}\cdot q_1 J_{21}\cdot\epsilon_1 - e_{2A}\cdot J_{21}\epsilon_1\cdot(p_2-p_1)] + 2\varepsilon_{\mu_1\mu_2\mu_3\mu_4} J_{21}^{\mu_2}[\epsilon_1\cdot\epsilon_2 q_1^{\mu_3} q_2^{\mu_1}(p_2-p_1)^{\mu_4} + (\epsilon_2\cdot q_1\epsilon_1^{\mu_1} - \epsilon_1\cdot q_2\epsilon_2^{\mu_1})\times(q_1+q_2)^{\mu_3}(p_2-p_1)^{\mu_4}]\frac{C_0(p_2-p_1, q_1+q_2, m_f)}{(q_1+q_2)^2}\Big\}. \quad (2.12)$$

Further expressions for amplitudes of graphs with a triangle insertion can be taken from [13] replacing e^μ_{iH} by $e^\mu_{iA}(m_f)$. The tensor structure of the box diagram in Fig. 1(b) is given by $\bar{B}_{\mu_1\mu_2\mu_3}(q_1, q_2, q_3, m_f)$, (see Appendix B, Fig. 11). Finally, the color structure of the $qg \to qgA$ amplitude is given by [13]

$$\mathcal{A}^{qg} = (t^{a_1}t^{a_2})_{i_2 i_1}\mathcal{A}^{qg}_{12} + (t^{a_2}t^{a_1})_{i_2 i_1}\mathcal{A}^{qg}_{21} \quad \text{with} \quad \mathcal{A}^{qg} = \sum_f \mathcal{A}^{qg}_f. \quad (2.13)$$

The indices 12 and 21 label amplitudes with interchanged external gluons. Thus, the resulting color-summed squared amplitude takes the form

$$\sum_{\text{color}} |\mathcal{A}^{qg}|^2 = (|\mathcal{A}^{qg}_{12}|^2 + |\mathcal{A}^{qg}_{21}|^2)\frac{(N^2-1)^2}{4N} - 2\,\text{Re}[\mathcal{A}^{qg}_{12}(\mathcal{A}^{qg}_{21})^*]\frac{N^2-1}{4N}. \quad (2.14)$$

3. Subprocesses $gg \to ggA$

After inserting suitable loop topologies and application of Furry's theorem, this process contains 19 graphs with triangle insertions, 18 box contributions and 12 pentagon diagrams. The pentagon diagrams, Fig. 1(c), enter via the $P^{\mu_1\mu_2\mu_3\mu_4}$ tensor (see Appendix C Fig. 12). Full expressions and diagrams can be looked up in [18]. The contributing color structures to the process $gg \to ggA$ can be expressed by the real-valued color coefficients c_i defined in [13]

$$c_1 = \mathrm{tr}[t^{a_1}t^{a_2}t^{a_3}t^{a_4}] + \mathrm{tr}[t^{a_1}t^{a_4}t^{a_3}t^{a_2}],$$
$$c_2 = \mathrm{tr}[t^{a_1}t^{a_3}t^{a_4}t^{a_2}] + \mathrm{tr}[t^{a_1}t^{a_2}t^{a_4}t^{a_3}], \quad (2.15)$$
$$c_3 = \mathrm{tr}[t^{a_1}t^{a_4}t^{a_2}t^{a_3}] + \mathrm{tr}[t^{a_1}t^{a_3}t^{a_2}t^{a_4}].$$

Evaluation of the color traces yields

$$c_1 = \frac{1}{4}\left(\frac{2}{N}\delta^{a_1a_2}\delta^{a_3a_4} + d^{a_1a_2l}d^{a_3a_4l} - f^{a_1a_2l}f^{a_3a_4l}\right),$$
$$c_2 = \frac{1}{4}\left(\frac{2}{N}\delta^{a_1a_3}\delta^{a_4a_2} + d^{a_1a_3l}d^{a_4a_2l} - f^{a_1a_3l}f^{a_4a_2l}\right), \quad (2.16)$$
$$c_3 = \frac{1}{4}\left(\frac{2}{N}\delta^{a_1a_4}\delta^{a_2a_3} + d^{a_1a_4l}d^{a_2a_3l} - f^{a_1a_4l}f^{a_2a_3l}\right).$$

In terms of these color coefficients, the complete amplitude for $gg \to ggA$ can be decomposed into three separately gauge invariant subamplitudes

$$\mathcal{A}^{gg} = \sum_{i=1}^{3} c_i \sum_f \mathcal{A}^{gg}_{i,f}. \quad (2.17)$$

The sum over colors of the external gluons for the squared amplitude becomes

$$\sum_{\text{color}} |\mathcal{A}^{gg}|^2 = \sum_{i,j=1}^{3} \mathcal{A}^{gg}_i (\mathcal{A}^{gg}_j)^* \sum_{\text{color}} c_i c_j, \quad (2.18)$$

where the color factors are given by

$$\mathcal{C}_1 \equiv \sum_{\text{color}} c_i c_i = \frac{(N^2-1)(N^4-2N^2+6)}{8N^2}, \quad (\text{no sum. over } i), \quad (2.19)$$

$$\mathcal{C}_2 \equiv \sum_{\text{color}} c_i c_j = \frac{(N^2-1)(3-N^2)}{4N^2}, \qquad i \neq j. \quad (2.20)$$

Thus, one finally gets

$$\sum_{\text{color}} |\mathcal{A}^{gg}|^2 = \mathcal{C}_1 \sum_{i=1}^{3} |\mathcal{A}^{gg}_i|^2 + \mathcal{C}_2 \sum_{i,j=1;i\neq j}^{3} \mathcal{A}^{gg}_i (\mathcal{A}^{gg}_j)^*. \quad (2.21)$$

III. NUMERICAL IMPLEMENTATION

Analytic expressions for the amplitudes of the previous chapter were implemented in the Fortran program *VBFNLO* [14]. The tensor reduction of the loop contributions up to boxes is performed via Passarino–Veltman reduction [19]. Additionally, we avoid the explicit calculation of the inverse of the Gram matrix by solving system of linear equations, which is numerically more stable close to the singular points. For pentagons, we use the Denner–Dittmaier algorithm [20] which avoids the inversion of small Gram determinants, in particular, for planar configurations of the Higgs and the two final-state partons. The program was numerically tested in several ways. Besides usual gauge-invariance and Lorentz-invariance tests of the amplitudes, the different topologies were checked separately. The contraction of a triangle-tensor $T_{\mu_1\mu_2}(q_1, q_2, m_f)$ with gluon momentum q_i^μ has to vanish due to total antisymmetry of the Levi-Civita symbol

$$q_1^{\mu_1} T_{\mu_1\mu_2}(q_1, q_2, m_f) = q_2^{\mu_2} T_{\mu_1\mu_2}(q_1, q_2, m_f) = 0. \quad (3.1)$$

Contracting with external gluon momenta, the tensor expressions of boxes and pentagons reduce to differences of triangles and boxes, respectively. With the tensor integrals as defined in the Appendix, the Ward identities for the boxes read

$$q_1^{\mu_1} B_{\mu_1\mu_2\mu_3}(q_1, q_2, q_3, m_f) = T_{\mu_2\mu_3}(q_{12}, q_3, m_f) - T_{\mu_2\mu_3}(q_2, q_3, m_f), \quad (3.2)$$

$$q_2^{\mu_2} B_{\mu_1\mu_2\mu_3}(q_1, q_2, q_3, m_f) = T_{\mu_1\mu_3}(q_1, q_{23}, m_f) - T_{\mu_1\mu_3}(q_{12}, q_3, m_f), \quad (3.3)$$

$$q_3^{\mu_3} B_{\mu_1\mu_2\mu_3}(q_1, q_2, q_3, m_f) = T_{\mu_1\mu_2}(q_1, q_2, m_f) - T_{\mu_1\mu_2}(q_1, q_{23}, m_f), \quad (3.4)$$

where the abbreviation $q_{ij} = q_i + q_j$ has been used. Similarly, for the pentagons, one finds

$$q_1^{\mu_1} P_{\mu_1\mu_2\mu_3\mu_4}(q_1, q_2, q_3, q_4, m_f) = B_{\mu_2\mu_3\mu_4}(q_{12}, q_3, q_4, m_f) - B_{\mu_2\mu_3\mu_4}(q_2, q_3, q_4, m_f), \quad (3.5)$$

$$q_2^{\mu_2} P_{\mu_1\mu_2\mu_3\mu_4}(q_1, q_2, q_3, q_4, m_f) = B_{\mu_1\mu_3\mu_4}(q_1, q_{23}, q_4, m_f) - B_{\mu_1\mu_3\mu_4}(q_{12}, q_3, q_4, m_f), \quad (3.6)$$

$$q_3^{\mu_3} P_{\mu_1\mu_2\mu_3\mu_4}(q_1, q_2, q_3, q_4, m_f) = B_{\mu_1\mu_2\mu_4}(q_1, q_2, q_{34}, m_f) - B_{\mu_1\mu_2\mu_4}(q_1, q_{23}, q_4, m_f), \quad (3.7)$$

$$q_4^{\mu_4} P_{\mu_1\mu_2\mu_3\mu_4}(q_1, q_2, q_3, q_4, m_f) = B_{\mu_1\mu_2\mu_3}(q_1, q_2, q_3, m_f) - B_{\mu_1\mu_2\mu_3}(q_1, q_2, q_{34}, m_f). \quad (3.8)$$

These relationships were tested numerically and they, typically, are satisfied at the 10^{-9} level when using Denner–Dittmaier reduction for the tensor integrals. In addition, one can perform a QED-check for the pentagons. Replacing gluons by photons and considering the process $\gamma\gamma \to \gamma\gamma A$, diagrams with three- and four-gluon-vertices vanish, because these structures are not available in an Abelian theory. The amplitude is simply given by the sum of all pentagon graphs, without color factors. When contracting with an external gauge boson momentum, one

obtains zero, since boxes are not allowed for photons, by Furry's theorem. Our amplitudes pass this test as well.

To check the full scattering amplitudes, one can make use of the heavy-top effective Lagrangian for a SM strength Yukawa coupling,

$$\mathcal{L}^A_{\text{eff}} = \frac{\alpha_s}{8\pi v} G^a_{\mu_1\mu_2} \tilde{G}^{a\mu_1\mu_2} A \quad \text{with}$$
$$\tilde{G}^{a\mu_1\mu_2} = \frac{1}{2}\epsilon^{\mu_1\mu_2\mu_3\mu_4} G^a_{\mu_3\mu_4}. \tag{3.9}$$

As m_t becomes large, the results calculated with full fermion loops must approach the approximate ones derived from the effective Lagrangian. This check was performed with $m_t = 5000$ GeV, and cross sections agree at the 1% level or better. In production runs, we put a cut in the routines for the determination of the tensor integral coefficients of the C and D functions such that the complete amplitude is set to zero when small Gram determinants appear. We have checked that the result and plots do not depend on this cut for a broad range of values. Finally, the amplitudes for all three subprocesses were recalculated using the *FeynCalc/FormCalc* framework [21]. For a selection of randomly generated phase space points, the two independent calculations yield agreement at least at the 10^{-6} level.

IV. APPLICATIONS TO LHC PHYSICS

The numerical analysis of the Φ + 2 jet cross section was performed with a parton level Monte Carlo program in the *VBFNLO* framework [14], using the CTEQ6L1 [22] set for parton-distribution functions. In order to prevent soft or collinear divergencies in the cross sections, a minimal set of acceptance cuts has to be introduced. Following Ref. [13], we impose

$$p_{Tj} > 20 \text{ GeV}, \qquad |\eta_j| < 4.5, \qquad R_{jj} > 0.6, \tag{4.1}$$

where p_{Tj} is the transverse momentum of a final state parton and R_{jj} describes the separation of the two partons in the pseudorapidity versus azimuthal-angle plane

$$R_{jj} = \sqrt{\Delta\eta^2_{jj} + \phi^2_{jj}}, \tag{4.2}$$

with $\Delta\eta_{jj} = |\eta_{j1} - \eta_{j2}|$ and $\phi_{jj} = \phi_{j1} - \phi_{j2}$. These cuts anticipate LHC detector capabilities and jet finding algorithms and will be called "inclusive cuts" (IC) in the following. Unless specified otherwise, the factorization scale is set to

$$\mu_f = \sqrt{p_{T1} p_{T2}}, \tag{4.3}$$

while the renormalization scale is fixed by setting [13]

$$\alpha_s^4(\mu_R) = \alpha_s(p_{T1})\alpha_s(p_{T2})\alpha_s^2(m_\Phi). \tag{4.4}$$

We use one-loop α_s running with $\alpha_s(M_Z) = 0.13$. All our results below contain the contributions from the full top- and bottom-quark loops. For the top-quark mass, we use $m_t = 173.1$ GeV. In the case of bottom-loops, running Yukawa coupling and propagator mass are taken into account, with the Higgs-mass as reference scale. Within the Higgs-mass range of 100–600 GeV, the bottom-quark mass is 33% to 42% smaller than the pole mass of 4.855 GeV. The evolution of m_b up to a reference scale μ can be expressed as

$$\bar{m}_b(\mu) = \bar{m}_b(m_b)\frac{c[\alpha_s(\mu)/\pi]}{c[\alpha_s(m_b)/\pi]}, \tag{4.5}$$

with $\bar{m}_b(m_b) = 4.2$ GeV, as derived from the relation between pole mass and MS-bar mass. For the coefficient function c, the five-flavor approximation [23,24] within the mass range $m_b < \mu < m_t$,

$$c(x) = \left(\frac{23}{6}x\right)^{12/23} \times [1 + 1.17549x + 1.50071x^2 + 0.172478x^3], \tag{4.6}$$

is used. Further evolution of $\bar{m}_b$ to a renormalization scale $\mu > m_t$ can be performed safely within the five-flavor approximation, because the deviation to the six-flavor scheme is less than 1% for $\mu < 600$ GeV.

Contributions of individual subprocess categories to the total cross section for $\tan\beta = 1$ are shown in Fig. 2 as a function of the Higgs boson mass, m_A. Here, the minimal cuts of Eq. (4.1) were used. The cross sections for processes involving gluons (quark-gluon or gluon-gluon amplitudes) exceed the quark-quark scattering contributions by more than one order of magnitude. The m_A dependence of the full cross section, with top- and bottom-quark interference, is given in the left panel of Fig. 3 for a selection of

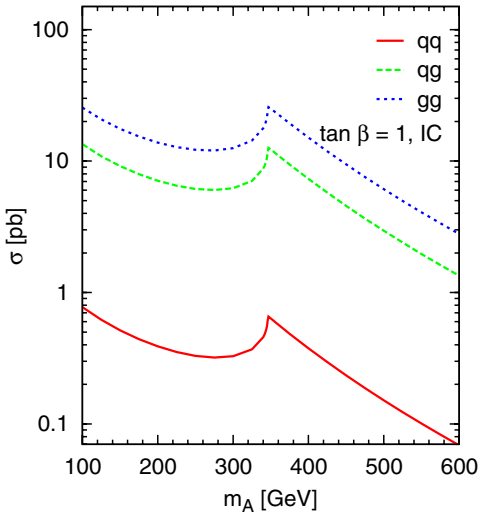

FIG. 2 (color online). $A + 2$ jet cross section of the individual contributions of the subprocesses quark-quark, quark-gluon and gluon-gluon scattering for tan $\beta = 1$ as a function of the pseudoscalar Higgs boson mass, m_A. Here, the inclusive cuts (IC) of Eq. (4.1) were applied.

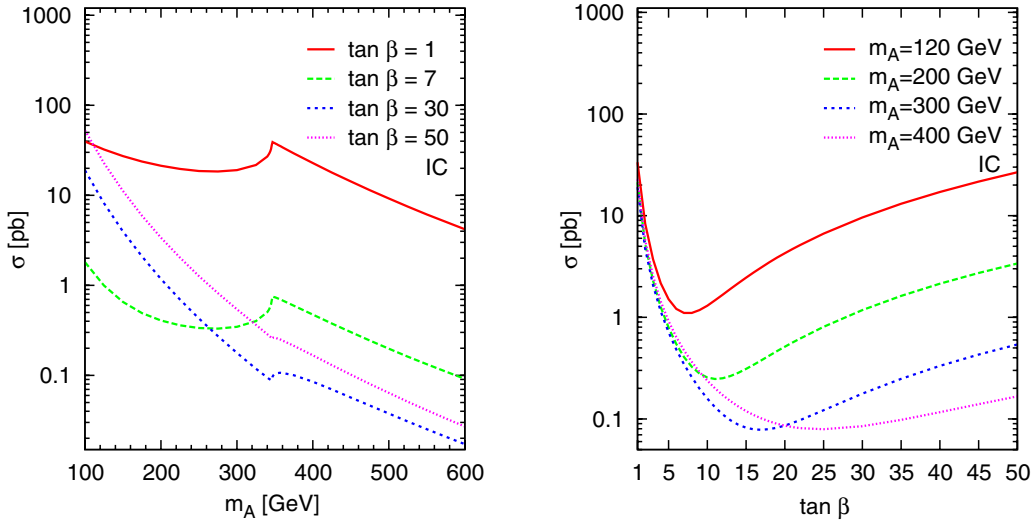

FIG. 3 (color online). $A + 2$ jet cross section as a function of the pseudoscalar Higgs boson mass, m_A for different values of tan β. The inclusive cuts (IC) of Eq. (4.1) are applied.

tanβ values. For small tanβ, amplitudes with a top-quark loop dominate over bottom-quark loop mediated contributions. The striking peak arises due to threshold enhancement near $m_A \approx 2m_t$, whereas for bottom-quark loop dominated processes, the peak would appear well below the Higgs mass range shown.

For low m_A, the minimal cross section is obtained near tan$\beta \approx 7$, when $h_t \approx h_b$ [see Eq. (2.3)] and both Yukawa couplings are suppressed compared to h_t^{SM}. For large tanβ, e.g. tan$\beta = 50$ in Fig. 3 (left panel), the bottom-quark loops dominate. However, they lead to a much more rapid decrease of the cross section with rising m_A because the suppression scale of the loops is now set by the heavy Higgs boson mass instead of the quark mass. The reduced importance of the bottom-quark loops at large m_A implies that equality of the top and bottom contributions and, thereby, the minimum of the production cross section is reached at increasingly larger tanβ as m_A is increased. This effect is demonstrated in the right panel of Fig. 3.

The γ_5-matrix in the Dirac-trace of the quark loops leads to a new tensor structure and to a normalization of the loops that, for equal Yukawa couplings, induces a $(3/2)^2 = 2.25$ times larger Ajj than Hjj cross section. This enhancement is shown in Fig. 4 and is also apparent in the effective Lagrangian of Eq. (1.1), where the coefficient of the $\mathcal{CP}$-odd Agg coupling exceeds that of the Hgg coupling by a factor $3/2$. This effective Lagrangian provides a good approximation to the total Φjj cross sections up to Higgs-masses of ≈ 160 GeV and for small transverse momenta, $p_{Tj} \lesssim m_t$. In this region, the effective Lagrangian approximation can be used as a numerically fast alternative for phenomenological studies [13].

The smaller quark mass in the bottom loops also has a pronounced effect on the transverse-momentum distribution of the accompanying jets: for $p_{Tj} \gtrsim m_b$ the large scale of the kinematic invariants leads to an additional suppression of the bottom induced subamplitudes compared to the heavy quark effective theory. This effect is clearly visible in Figs. 5 and 6, where the transverse-momentum distributions of the softer and the harder of the two jets are shown for pseudoscalar Higgs masses $m_A =$ 120, 200 and 400 GeV for tan$\beta = 1$, 7, 30. For modest Higgs mass values, both distributions fall more steeply for large tanβ. At large values of m_A, the Higgs boson mass sets the scale for the fermion loops which, in the $m_A =$ 400 GeV panels of Figs. 5 and 6, leads to p_T distributions which are approximately equal for the top- or bottom-quark dominated loops. Similar effects are observed in the dijet-invariant mass distribution, Fig. 7. From Figs. 5–7, we confirm similarly to the CP-even Higgs case, that the

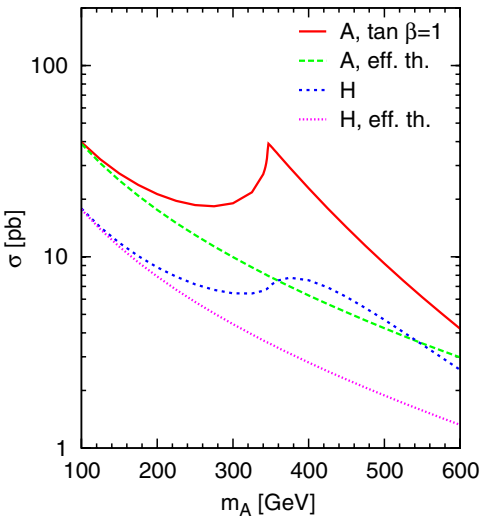

FIG. 4 (color online). Comparison of cross sections for the $\mathcal{CP}$-odd and $\mathcal{CP}$-even Higgs for the full loop calculation and within the effective theory. The inclusive cuts (IC) of Eq. (4.1) are applied.

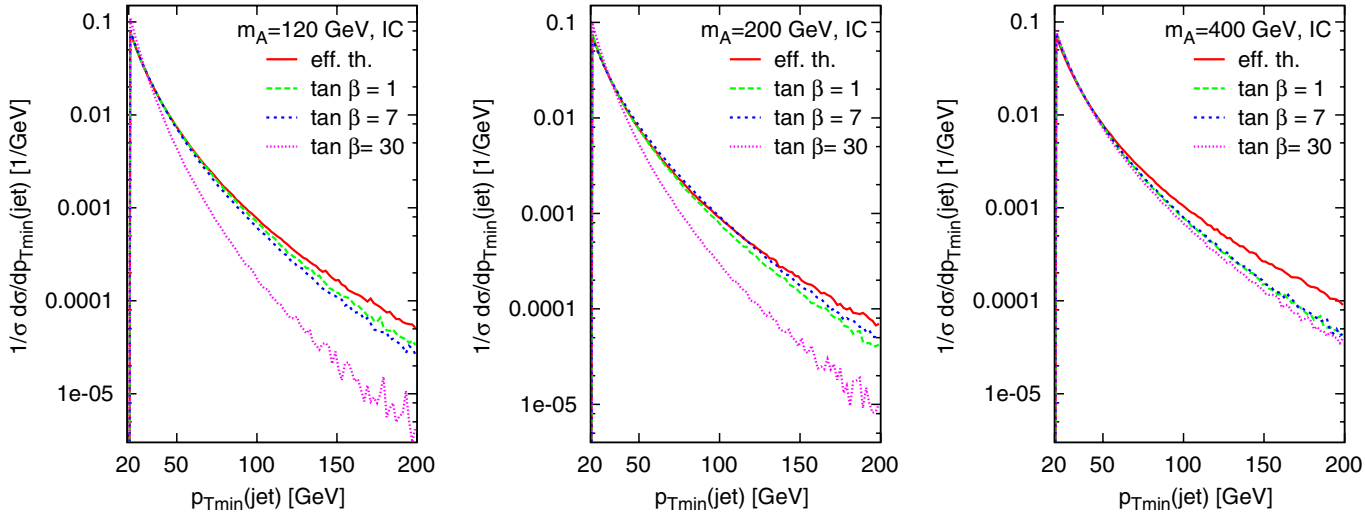

FIG. 5 (color online). Normalized transverse-momentum distributions of the softer jet in Ajj production at the LHC, for different tan β and Higgs-mass values. The inclusive selection cuts of Eq. (4.1) are applied.

validity of the heavy quark mass approximation is restricted to $m_\phi < m_q$ and $p_{Tj} < m_q$, while large dijet-invariant masses do not spoil the validity of this limit.

For the set of pseudoscalar Higgs masses and tanβ values mentioned above, predictions for the normalized ϕ_{jj}-distributions are shown in Fig. 8. The calculation was carried out with a modified set of cuts, however, which was shown in Ref. [29] to lead to a better sensitivity to the $\mathcal{CP}$-structure of the Higgs couplings than the inclusive cuts. In Fig. 8, we use

$$p_{Tj} > 30 \text{ GeV}, \qquad |\eta_j| < 4.5, \qquad R_{jj} > 0.6, \qquad \Delta\eta_{jj} = |\eta_{j1} - \eta_{j2}| > 3, \tag{4.7}$$

which we call ICphi cuts in the following. One finds that the characteristic structure of the ϕ_{jj} distribution dips at $\phi_{jj} = 0$ and $\phi_{jj} = \pm 180$ degrees, and remains there for bottom-quark dominated Ajj production, albeit at a quantitatively reduced level for $m_A > 2m_q$. For a relatively light pseudoscalar Higgs boson and large tanβ, the softer transverse-momentum distribution of the Higgs leads to kinematical distortions of the ϕ_{jj} distribution: at $\phi_{jj} \approx 0$ the Higgs recoils against two jets and hence must have $p_{TH} > 60$ GeV, and this high p_T-scale leads to an additional suppression as compared to the $\phi_{jj} \approx \pm 180$ degree case where transverse-momentum balancing of the jets does allow $p_{TH} = 0$.

The azimuthal angle between the more forward and the more backward of the two tagging jets, $\phi_{jj} = \phi_{jF} - \phi_{jB}$, provides a sensitive probe for the $\mathcal{CP}$-character of the Higgs couplings to the quarks [25–28,35]. As shown in the left panel of Fig. 9, for a heavy quark in the loop, the

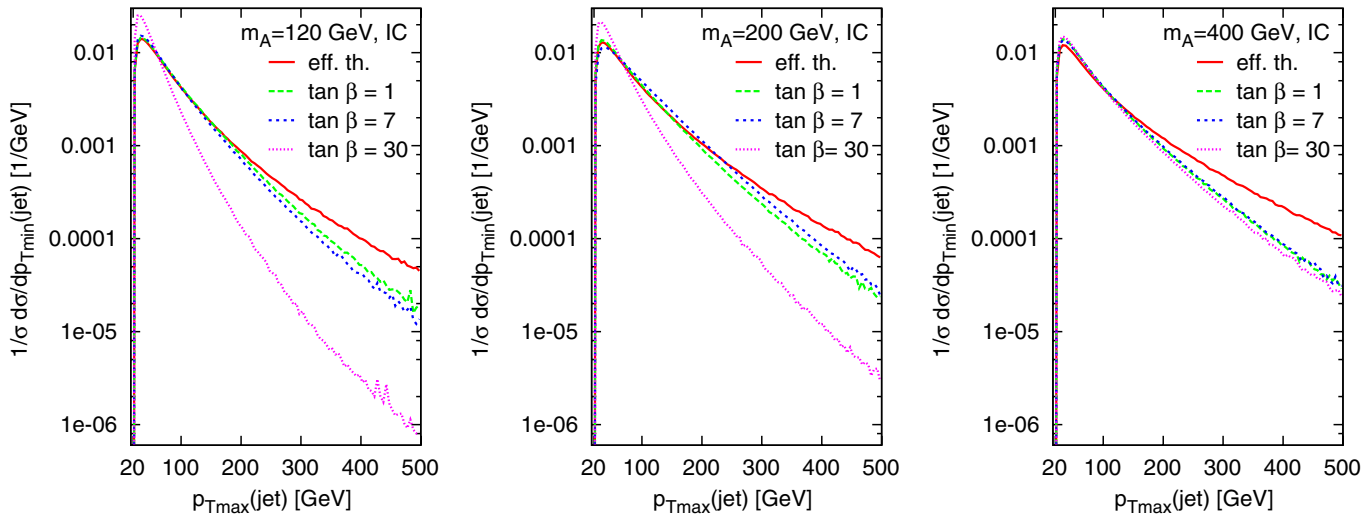

FIG. 6 (color online). Normalized transverse-momentum distributions of the harder jet in Ajj production at the LHC for different tan β and Higgs-mass values. The inclusive selection cuts of Eq. (4.1) are applied.

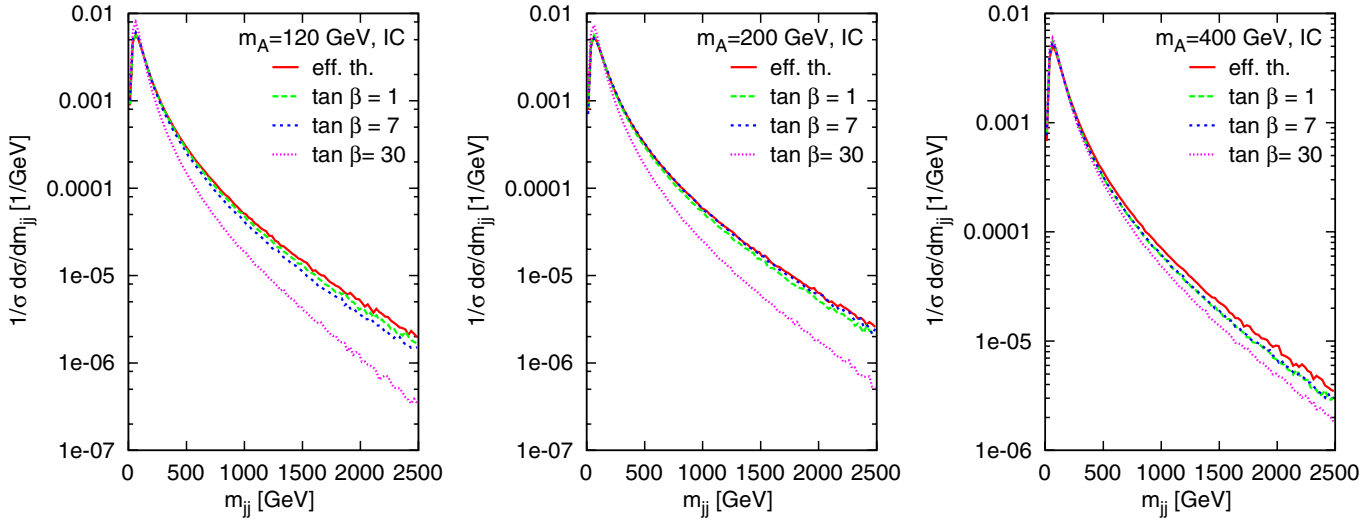

FIG. 7 (color online). Normalized dijet-invariant mass distributions in Ajj production at the LHC for different tan and Higgs-mass values. The inclusive selection cuts of Eq. (4.1) are applied.

$\mathcal{CP}$-even Hqq coupling produces a minimum for $\phi_{jj} = \pm 90$ degrees while a γ_5-induced $\mathcal{CP}$-odd Aqq coupling leads to minima at $\phi_{jj} = 0$ and ± 180 degrees. The softening effects observed for the jet transverse-momentum distribution then raise the question, to what extent the jet azimuthal-angle correlations of the effective theory will get modified when bottom-quark loops dominate.

For the effective theory of the large quark mass limit, it was observed that $\mathcal{CP}$-violating effects due to a mixture of $\mathcal{CP}$-even and $\mathcal{CP}$-odd couplings leads to a phase shift of the ϕ_{jj} distribution compared to the $\mathcal{CP}$-even case by an angle, α, which is given by the relative strength of the two couplings [26,27]. Taking into account the relative enhancement by the factor $3/2$ of the Agg coupling due to loop effects, the phase shift angle is given by

$$\tan\alpha = \frac{3}{2}\frac{\tilde{y}_q}{y_q}, \tag{4.8}$$

when heavy quark loops of a single flavor dominate. In order to test this effect for the case of a light quark, we show, in the right panel of Fig. 9, the results for

$$y_b = \frac{3}{2}\tilde{y}_b = -\tan\beta\frac{m_b}{v} \quad \text{and} \quad y_t = \frac{3}{2}\tilde{y}_t = -\cot\beta\frac{m_t}{v}, \tag{4.9}$$

where a 45° phase shift is expected, with minima of the ϕ_{jj} distribution at $-45°$ and $+135°$. This basic expectation is,

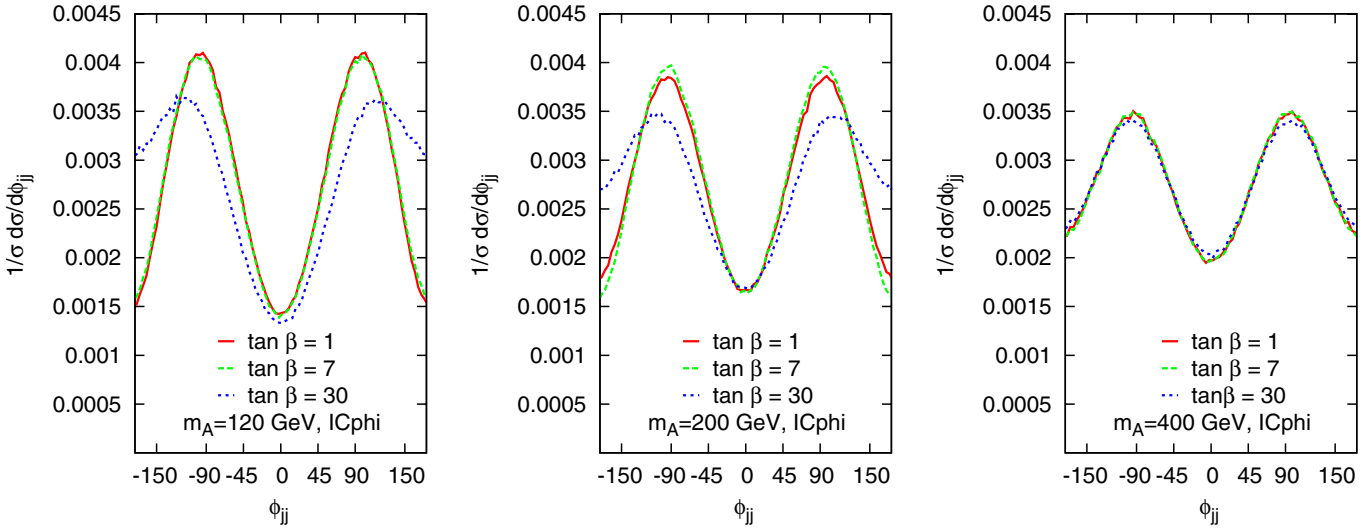

FIG. 8 (color online). Distribution in the azimuthal-angle between the two final state jets for $\mathcal{CP}$-odd Higgs boson production at different Higgs-masses and tan values. The ICphi set of acceptance cuts [see Eq. (4.7)] is used for pp collisions at 14 TeV.

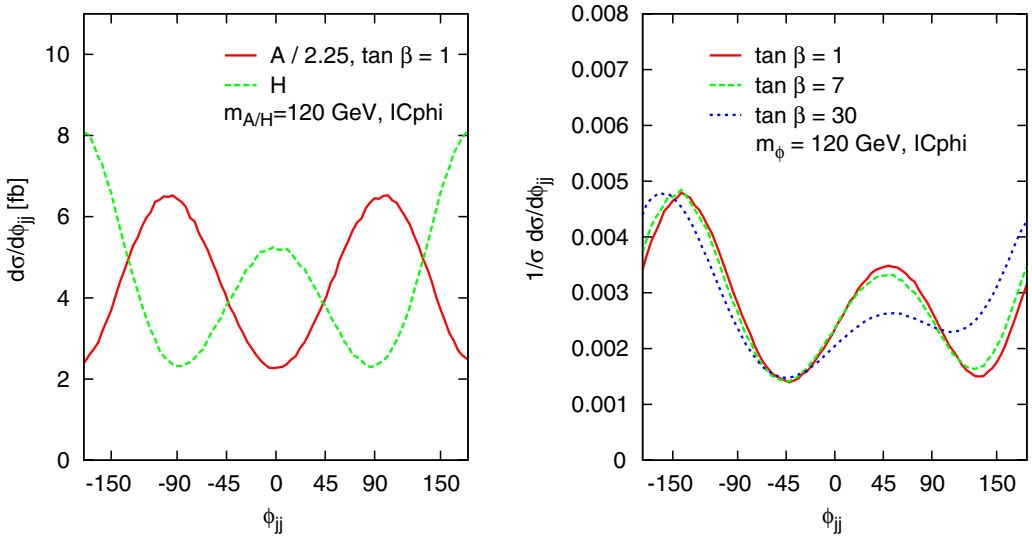

FIG. 9 (color online). ϕ_{jj} distributions for different Higgs-sector scenarios: pure $\mathcal{CP}$-odd or $\mathcal{CP}$-even coupling in the effective Lagrangian limit (left panel) and the $\mathcal{CP}$- violating case defined in Eq. (4.9) (right panel). In the effective Lagrangian, the $\mathcal{CP}$-odd coupling was matched to the $\mathcal{CP}$-even coupling by a factor $2/3$. For the $\mathcal{CP}$-violating Higgs-sector, results are shown for different tan values. Here, the ICphi set (4.7) was applied for both panels.

indeed, confirmed by the detailed calculation. However, there are additional distortions of the azimuthal-angle distributions which can again be explained by kinematical effects due to transverse-momentum balancing of the two jets and the Higgs boson.

The azimuthal-angle correlations of the jets will be affected by higher-order QCD corrections, in particular, due to the emission of additional partons. When considering large rapidity separations of the two leading jets, decorrelation effects may be expected to be particularly large, due to the increased phase space for such emissions. Indeed, parton shower studies of such effects [30,31] at first seemed to indicate such decorrelations which, however, are likely due to approximations made in the parton shower treatment. For the effective theory, also the NLO QCD corrections for hjj production are available, and they do not indicate a significant decorrelation of the jet azimuthal angles [32]. This result is strengthened by a recent analysis of hjj distributions with multiple parton emissions in a framework which correctly models the high energy limit of the QCD amplitudes [33]. Encouraged by these results, we assume that also for the more general situation considered here, with significant contributions from light (bottom) quark loops, the azimuthal-angle distributions will not be significantly distorted by additional parton emission. An actual study of these questions is beyond the scope of the present paper, however.

V. CONCLUSIONS

In this paper, we have presented the determination of quark mass effects on the cross section and on distributions for pseudoscalar Higgs production in association with two final state partons. Our calculation for Ajj production complements the analogous one for a scalar Higgs, i.e. Hjj production as carried out in Ref. [13]. Qualitative features are quite similar for the two cases. Validity of the heavy quark mass approximation is found to be restricted to $m_\Phi < m_q$ and $p_{Tj} < m_q$ while large dijet-invariant masses do not spoil the validity of the heavy quark limit. A pronounced difference between Ajj and Hjj production is observed in the azimuthal-angle distribution between the two jets, which allows, in principle, to determine the $\mathcal{CP}$-properties of the produced Higgs boson at the LHC [27].

Our analytical expressions have been implemented in the VBFNLO program [14] and are publicly available as a parton level Monte Carlo program. Even though the code must evaluate loop expressions up to pentagons, the calculation is leading order in the strong coupling constant since Higgs production in gluon fusion first appears at the one-loop level. As a leading order process, it has been provided with an interface in the Les Houches format [34] to run with parton shower programs, providing full particle, momentum, and color flow information. The code allows to sum top- and bottom-quark induced contributions with arbitrary $\mathcal{CP}$-violating couplings

$$\mathcal{L}_{\text{Yukawa}} = \bar{q}(y_q + i\gamma_5 \tilde{y}_q) q \Phi, \tag{5.1}$$

and, thus, is versatile enough for simulating the effects of general, $\mathcal{CP}$-violating Higgs sectors at the LHC.

ACKNOWLEDGMENTS

We would like to thank Gunnar Klämke for helpful discussions, and Christian Schappacher, for the comparison with the *FeynArts/FormCalc* [21] framework. This research was supported in part by the Deutsche Forschungsgemeinschaft via the Sonderforschungsbereich/Transregio SFB/TR- 9 âComputational Particle Physicsâ. M. K. gratefully acknowledges support of the Graduiertenkolleg "High Energy Physics and Particle Astrophysics" and Landesgraduiertenförderung Baden-Württemberg. F. C acknowledges partial support by FEDER and Spanish MICINN under Grant No. FPA2008-02878.

APPENDIX A: TENSOR STRUCTURE OF TRIANGLES

The generic three-point functions for triangle graphs with opposite loop momentum have the following expressions

$$T_1^{\mu_1\mu_2}(q_1, q_2, m_f) = \frac{-\mathrm{i}}{4m_f}\int\frac{d^4k}{\mathrm{i}\pi^2}\,\mathrm{tr}\Big[\frac{\not k + m_f}{k^2-m_f^2}\gamma^{\mu_1}\frac{\not k + \not q_1 + m_f}{(k+q_1)^2-m_f^2} \times \gamma^{\mu_2}\frac{\not k + \not q_{12} + m_f}{(k+q_{12})^2-m_f^2}\gamma^5\Big], \tag{A1}$$

$$T_2^{\mu_1\mu_2}(q_1, q_2, m_f) = \frac{-\mathrm{i}}{4m_f}\int\frac{d^4k}{\mathrm{i}\pi^2}\,\mathrm{tr}\Big[\frac{+m_f}{k^2-m_f^2}\gamma^{\mu_2}\frac{\not k + \not q_2 + m_f}{(k+q_2)^2-m_f^2} \times \gamma^{\mu_1}\frac{\not k + \not q_{12} + m_f}{(k+q_{12})^2-m_f^2}\gamma^5\Big], \tag{A2}$$

where q_1, q_2 are outgoing momenta, $q_{12} = q_1 + q_2$ and the overall factor $-\mathrm{i}/4m_f$ cancels the explicit mass factor arising from the Dirac trace. Using the charge-conjugation matrix C

$$\hat C\gamma_\mu\hat C^{-1} = -\gamma_\mu^T, \qquad \hat C\gamma_5\hat C^{-1} = \gamma_5^T \quad \text{with} \qquad \hat C = \gamma^0\gamma^2, \qquad \hat C^2 = \mathbb{1}, \tag{A3}$$

one can derive (Furry's theorem [16])

$$T_1^{\mu_1\mu_2}(q_1, q_2, m_f) = T_2^{\mu_1\mu_2}(q_1, q_2, m_f) \equiv T^{\mu_1\mu_2}(q_1, q_2, m_f). \tag{A4}$$

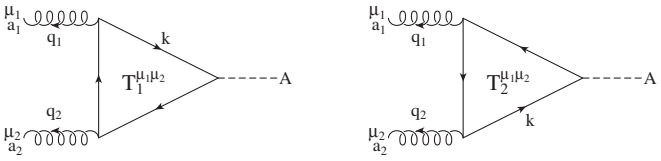

FIG. 10. Two three-point functions connected by charge conjugation.

Thus, the color structure simplifies to

$$\mathrm{tr}[t^{a_1}t^{a_2}]T_1^{\mu_1\mu_2}(q_1, q_2, mq) + \mathrm{tr}[t^{a_2}t^{a_1}]T_2^{\mu_1\mu_2}(q_1, q_2, m_f) = \delta^{a_1a_2}T^{\mu_1\mu_2}(q_1, q_2, m_f). \tag{A5}$$

Evaluation of the Dirac trace yields

$$T^{\mu_1\mu_2}(q_1, q_2, m_f) = \varepsilon^{\mu_1\mu_2q_1q_2}C_0(q_1, q_2, m_f). \tag{A6}$$

Here, C_0 denotes the scalar three-point function and $\varepsilon^{\mu\nu q_1 q_2}$ is the totally antisymmetric tensor (Levi-Civita symbol), contracted with the gluon momenta q_1 and q_2.

APPENDIX B: TENSOR STRUCTURE OF BOXES

The analytic expressions for the charge-conjugated boxes are

$$\bar B_1^{\mu_1\mu_2\mu_3}(q_1, q_2, q_3, m_f) = \frac{-\mathrm{i}}{4m_f}\int\frac{d^4k}{\mathrm{i}\pi^2}\,\mathrm{tr}\Big[\frac{\not k + m_f}{k^2-m_f^2}\gamma^{\mu_1}\frac{\not k + \not q_1 + m_f}{(k+q_1)^2-m_f^2} \times \gamma^{\mu_2}\frac{\not k + \not q_{12} + m_f}{(k+q_{12})^2-m_f^2}\gamma^{\mu_3}\frac{\not k + \not q_{123} + m_f}{(k+q_{123})^2-m_f^2}\gamma^5\Big], \tag{B1}$$

$$\bar B_2^{\mu_1\mu_2\mu_3}(q_1, q_2, q_3, m_f) = \frac{-\mathrm{i}}{4m_f}\int\frac{d^4k}{\mathrm{i}\pi^2}\,\mathrm{tr}\Big[\frac{k + m_f}{k^2-m_f^2}\gamma^{\mu_3}\frac{\not k + \not q_3 + m_f}{(k+q_3)^2-m_f^2} \times \gamma^{\mu_2}\frac{\not k + \not q_{23} + m_f}{(k+q_{23})^2-m_f^2}\gamma^{\mu_1}\frac{\not k + \not q_{123} + m_f}{(k+q_{123})^2-m_f^2}\gamma^5\Big], \tag{B2}$$

where q_1, q_2 and q_3 are outgoing momenta, $q_{ij} = q_i + q_j$ and $q_{ijk} = q_i + q_j + q_k$. From charge conjugation one gets

$$\bar B_1^{\mu_1\mu_2\mu_3}(q_1, q_2, q_3, m_f) = -\bar B_2^{\mu_1\mu_2\mu_3}(q_1, q_2, q_3, m_f) \equiv \bar B^{\mu_1\mu_2\mu_3}(q_1, q_2, q_3, m_f). \tag{B3}$$

Two additional permutations are obtained by cyclic permutation of (1, 2, 3). The color structure for the sum of the two diagrams is

$$\begin{aligned}&\mathrm{tr}(t^{a_1}t^{a_2}t^{a_3})\bar B_1^{\mu_1\mu_2\mu_3}(q_1, q_2, q_3, m_f) + \mathrm{tr}(t^{a_3}t^{a_2}t^{a_1})\bar B_2^{\mu_1\mu_2\mu_3}(q_1, q_2, q_3, m_f)\\ &= [\mathrm{tr}(t^{a_1}t^{a_2}t^{a_3}) - \mathrm{tr}(t^{a_3}t^{a_2}t^{a_1})]\bar B^{\mu_1\mu_2\mu_3}(q_1, q_2, q_3, m_f)\\ &= \frac{\mathrm{i}}{2}f^{a_1a_2a_3}\bar B^{\mu_1\mu_2\mu_3}(q_1, q_2, q_3, m_f).\end{aligned} \tag{B4}$$

The tensor structure of charge-conjugation related box diagrams, e.g. with gluon permutation (1, 2, 3), can be written as

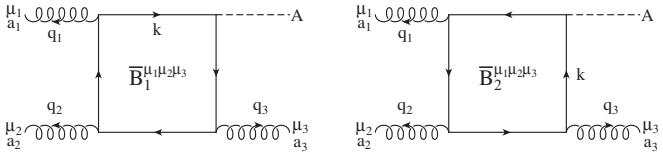

FIG. 11. Two four-point functions connected by charge conjugation.

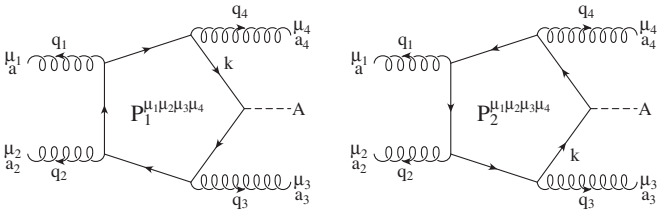

FIG. 12. Two five-point functions connected by charge conjugation.

$$\begin{aligned}\bar{B}^{\mu_1\mu_2\mu_3}(q_1,q_2,q_3,m_f) = \{&\varepsilon^{\mu_3 q_1 q_2 q_3} g^{\mu_1\mu_2} - \varepsilon^{\mu_2 q_1 q_2 q_3} g^{\mu_1\mu_3} + \varepsilon^{\mu_2\mu_3 q_2 q_3} q_1^{\mu_1} - \varepsilon^{\mu_2\mu_3 q_1 q_3} q_2^{\mu_1} + \varepsilon^{\mu_2\mu_3 q_1 q_2} q_3^{\mu_1}\\ &+ \varepsilon^{\mu_1 q_1 q_2 q_3} g^{\mu_2\mu_3} + \varepsilon^{\mu_1\mu_3 q_2 q_3} q_1^{\mu_2} - \varepsilon^{\mu_1\mu_3 q_1 q_2} q_3^{\mu_2} - \varepsilon^{\mu_1\mu_2 q_2 q_3} q_1^{\mu_3} + \varepsilon^{\mu_1\mu_2 q_1 q_3} q_2^{\mu_3}\\ &+ \varepsilon^{\mu_1\mu_2\mu_3 q_3} g^{\mu_1\mu_2} - \varepsilon^{\mu_1\mu_2\mu_3 q_2} g^{\mu_1\mu_3} + \varepsilon^{\mu_1\mu_2\mu_3 q_1} g^{\mu_2\mu_3} + \varepsilon^{\mu_1\mu_3 q_1 q_3}(2q_1^{\mu_2} + q_2^{\mu_2})\\ &+ \varepsilon^{\mu_1\mu_2 q_1 q_2}[2(q_1^{\mu_3} + q_2^{\mu_3}) + q_3^{\mu_3}]\}D_0(q_1,q_2,q_3,m_f) - \varepsilon^{\mu_1\mu_2\mu_3 q_3} C_0(q_1+q_2,q_3,m_f)\\ &- \varepsilon^{\mu_1\mu_2\mu_3 q_1} C_0(q_1,q_2+q_3,m_f) + 2\varepsilon^{\mu_2\mu_3 q_2 q_3} D^{\mu_1}(q_1,q_2,q_3,m_f)\\ &+ 2\varepsilon^{\mu_1\mu_3 q_1 q_3} D^{\mu_2}(q_1,q_2,q_3,m_f) + 2\varepsilon^{\mu_1\mu_2 q_1 q_2} D^{\mu_3}(q_1,q_2,q_3,m_f). \end{aligned} \tag{B5}$$

The D_0 and D_μ are four-point functions. Whereas the former denotes a scalar function, the latter can be expressed by the usual Passarino–Veltman decomposition [19] as

$$D^\mu(q_1,q_2,q_3,m_f) = q_1^\mu D_{11} + q_2^\mu D_{12} + q_3^\mu D_{13}. \tag{B6}$$

Note that after contraction with polarization vectors $\epsilon_1^{\mu_1}$, $\epsilon_2^{\mu_2}$ and quark current $J_{21}^{\mu_3}$, the expression (B5) still contains terms with factors $(\epsilon_1 \cdot q_1)$, $(\epsilon_2 \cdot q_2)$, $(J_{21} \cdot q_3)$ even though they vanish, since gluon-polarization vectors ϵ_i^μ and momenta q_i^μ are perpendicular to each other and the quark current J_{21} is conserved. However, these terms are important for numerical gauge checks, where the corresponding gluon-polarization vector is replaced by its momentum. Since the virtual gluon has a nonzero q_i^2, these terms give finite contributions.

APPENDIX C: TENSOR STRUCTURE OF PENTAGONS

The two five-point functions connected by charge conjugation are defined by the expressions 0

$$\begin{aligned}P_1^{\mu_1\mu_2\mu_3\mu_4}(q_1,q_2,q_3,q_4,m_f) = \frac{-\mathrm{i}}{4m_f}\int\frac{d^4k}{\mathrm{i}\pi^2}\,\mathrm{tr}\Big[&\frac{\not k + m_f}{k^2-m_f^2}\gamma^{\mu_4}\frac{\not k + \not q_4 q_4 + m_f}{(k+q_4)^2-m_f^2}\gamma^{\mu_1}\\ &\times\frac{\not k + \not q_{14} q_{14} + m_f}{(k+q_{14})^2-m_f^2}\gamma^{\mu_2}\frac{\not k + \not q_{124} + m_f}{(k+q_{124})^2-m_f^2}\gamma^{\mu_3}\frac{\not k + \not q_{1234} + m_f}{(k+q_{1234})^2-m_f^2}\gamma^5\Big],\end{aligned} \tag{C1}$$

$$\begin{aligned}P_2^{\mu_1\mu_2\mu_3\mu_4}(q_1,q_2,q_3,q_4,m_f) = \frac{-\mathrm{i}}{4m_f}\int\frac{d^4k}{\mathrm{i}\pi^2}\,\mathrm{tr}\Big[&\frac{\not k + m_f}{k^2-m_f^2}\gamma^{\mu_3}\frac{\not k + \not q_3 + m_f}{(k+q_3)^2-m_f^2}\gamma^{\mu_2}\\ &\times\frac{\not k + \not q_{23} + m_f}{(k+q_{23})^2-m_f^2}\gamma^{\mu_1}\frac{\not k + \not q_{123} + m_f}{(k+q_{123})^2-m_f^2}\gamma^{\mu_4}\frac{\not k + \not q_{1234} + m_f}{(k+q_{1234})^2-m_f^2}\gamma^5\Big],\end{aligned} \tag{C2}$$

where q_1, q_2, q_3 and q_4 are outgoing momenta ($q_{ij} = q_i + q_j$ and similarly for q_{ijk} and q_{ijkl}). The allowed color structures are given in [13]. The pentagon was reduced using the Denner–Dittmaier algorithm [20] and is available as a FORTRAN-subroutine in *VBFNLO* [14]. The full analytic expression in terms of Passarino–Veltman reduction can be found in [18].

[1] G. L. Bayatian *et al.* (CMS Collaboration) CMS physics: Technical design report.

[2] ATLAS Detector and Physics Performance. Technical Design Report. Vol. 2, CERN-LHCC-99-15, ATLAS-TDR-15, CERN, 1996.

[3] A. Djouadi, Phys. Rep. **459**, 1 (2008).

[4] D. Zeppenfeld, *et al.*, Phys. Rev. D **62**, 013009 (2000).

[5] M. Duhrssen *et al.*, Phys. Rev. D **70**, 113009 (2004).

[6] D. L. Rainwater and D. Zeppenfeld, J. High Energy Phys. 12 (1997) 005; D. L. Rainwater, D. Zeppenfeld, and K. Hagiwara, Phys. Rev. D **59**, 014037 (1998); D. L. Rainwater and D. Zeppenfeld, Phys. Rev. D **60**, 113004 (1999); **61**, 099901(E) (2000).

[7] J. R. Ellis, M. K. Gaillard, and D. V. Nanopoulos, Nucl. Phys. **B106**, 292 (1976).

[8] M. A. Shifman, *et al.*, Yad. Fiz. **30**, 1368 (1979) [Sov. J. Nucl. Phys. **30**, 711 (1979).

[9] S. Dawson, Nucl. Phys. **B359**, 283 (1991).

[10] A. Djouadi, M. Spira, and P. M. Zerwas, Phys. Lett. B **264**, 440 (1991).

[11] R. P. Kauffman, S. V. Desai, and D. Risal, Phys. Rev. D **55**, 4005 (1997); **58**, 119901(E) (1998).

[12] R. P. Kauffman and S. V. Desai, Phys. Rev. D **59**, 057504 (1999).

[13] V. Del Duca, *et al.*, Phys. Rev. Lett. **87**, 122001 (2001); Nucl. Phys. **B616**, 367 (2001).

[14] K. Arnold *et al.*, Comput. Phys. Commun. **180**, 1661 (2009); K. Arnold *et al.*, arXiv:1107.4038; The VBFNLO code can be obtained from, http://www-itp.particle.uni-karlsruhe.de/vbfnlo/

[15] J. F. Gunion, H. E. Haber, G. L. Kane, and S. Dawson, *The Higgs Hunter's Guide* (Addison-Wesley, Reading, USA, 1990).

[16] W. H. Furry, Phys. Rev. **51**, 125 (1937).

[17] K. Hagiwara and D. Zeppenfeld, Nucl. Phys. **B313**, 560 (1989).

[18] M. Kubocz, Diploma thesis (german), Institut für Theoretische Physik, Universität Karlsruhe, 2006, http://-www-itp.particle.uni-karlsruhe.de/diplomatheses.de.shtml.

[19] G. Passarino and M. J. G. Veltman, Nucl. Phys. **B160**, 151 (1979).

[20] A. Denner and S. Dittmaier, Nucl. Phys. **B658**, 175 (2003); Nucl. Phys. **B734**, 62 (2006).

[21] T. Hahn, Comput. Phys. Commun. **140**, 418 (2001); T. Hahn and C. Schappacher, Comput. Phys. Commun. **143**, 54(2002); T. Hahn and M. Perez-Victoria, Comput. Phys. Commun. **118**, 153 (1999).

[22] J. Pumplin, *et al.*, and , J. High Energy Phys. 07 (2002) 012.

[23] M. Spira, Fortschr. Phys. **46**, 203 (1998).

[24] J. A. M. Vermaseren, S. A. Larin, and T. van Ritbergen, Phys. Lett. B **405**, 327 (1997).

[25] T. Plehn, D. L. Rainwater, and D. Zeppenfeld, Phys. Rev. Lett. **88**, 051801 (2002).

[26] V. Hankele, *et al.*, Phys. Rev. D **74**, 095001 (2006).

[27] G. Klamke and D. Zeppenfeld, J. High Energy Phys. 04 (2007) 052.

[28] K. Hagiwara, Q. Li, and K. Mawatari, J. High Energy Phys. 07 (2009) 101.

[29] G. Klamke and D. Zeppenfeld, arXiv:0705.2983.

[30] K. Odagiri, J. High Energy Phys. 03 (2003) 009.

[31] V. Del Duca *et al.*, J. High Energy Phys. 10 (2006) 016.

[32] J. M. Campbell, R. K. Ellis, and G. Zanderighi, J. High Energy Phys. 10 (2006) 028.

[33] J. R. Andersen, K. Arnold, and D. Zeppenfeld, J. High Energy Phys. 06 (2010) 091.

[34] E. Boos *et al.*, [arXiv:hep-ph/0109068; J. Alwall *et al.*, Comput. Phys. Commun. **176**, 300 (2007).

[35] V. Hankele, G. Klamke, and D. Zeppenfeld, arXiv:hep-ph/0605117.